inorganics

MDPI

Article

Understanding Factors that Control the Structural (Dis)Assembly of Sulphur-Bridged Bimetallic Sites

Riyadh Alrefai, Henri Eggenweiler, Hartmut Schubert and Andreas Berkefeld *

Institut für Anorganische Chemie, Eberhard Karls Universität Tübingen, Auf der Morgenstelle 18, 72076 Tübingen, Germany; riyadh.alrefai@student.uni-tuebingen.de (R.A.); tim-henri.eggenweiler@student.uni-tuebingen.de (H.E.); hartmut.schubert@uni-tuebingen.de (H.S.)

* Correspondence: andreas.berkefeld@anorg.uni-tuebingen.de; Tel.: +49-(0)7071-29-76213

Received: 19 February 2019; Accepted: 13 March 2019; Published: 27 March 2019

Abstract: Bimetallic structures of the general type $[M_2(\mu\text{-}S)_2]$ are omnipresent in nature, for biological function $[M_2(\mu\text{-}S)_2]$ sites interconvert between electronically distinct, but isostructural, forms. Different from structure-function relationships, the current understanding of the mechanism of formation and persistence of $[M_2(\mu\text{-}S)_2]$ sites is poorly developed. This work reports on bimetallic model compounds of nickel that interconvert between functional structures $[Ni_2(\mu\text{-}S)_2]^{+/2+}$ and isomeric congeners $[2\{\kappa\text{-}S\text{–}Ni\}]^{2+/+}$, S = Aryl-$S^-$, in which the nickel ions are geometrically independent. Interconversion of the two sets of structures was studied quantitatively by UV–VIS absorption spectroscopy and cyclic voltammetry. Assembly of the $[Ni_2(\mu\text{-}S)_2]^+$ core from $[2\{\kappa\text{-}S\text{–}Ni\}]^+$ is thermodynamically and kinetically highly preferred over the disassembly of $[Ni_2(\mu\text{-}S)_2]^{2+}$ into $[2\{\kappa\text{-}S\text{–}Ni\}]^{2+}$. Labile Ni-$\eta^{2/3}$-bonding to aromatic π-systems of the primary thiophenol ligand is critical for modeling (dis)assembly processes. A phosphine coligand mimics the role of anionic donors present in natural sites that saturate metal coordination. Three parameters have been identified as critical for structure formation and persistence. These are, first, the stereoelectronic properties of the metals ions, second, the steric demand of the coligand, and, third, the properties of the dative bond between nickel and coligand. The energies of transition states connecting functional and precursor forms have been found to depend on these parameters.

Keywords: bimetallic complexes; nickel; thiolate ligands; kinetic study; electrochemistry; structure-function relationship

1. Introduction

Sulphur-bridged bimetallic structures of the general formula $[M_2(\mu\text{-}S)_2]$ present a recurring motif in natural metalloproteins that is associated in a variety of biological processes, including reversible bond making and breaking, electron transfer, and cellular regulation. The prominence of $[M_2(\mu\text{-}S)_2]$ sites in nature likely derives from the intriguing properties of the bond between metal and sulphur, be it inorganic sulfide or organic thiolate. The covalent character of an M–S bond varies sensitively with effective core charge and d-electron count of the metal. In-depth studies on Cu and Fe containing bimetallic Cu_A [1,2] and 2Fe-ferredoxins [3] disclosed that it is the degree of covalent bonding that determines the mechanism and strength of electronic coupling of the metals in these archetypal $[M_2(\mu\text{-}S)_2]$ structures [2]. As drawn in Figure 1, Cu_A and 2Fe-ferredoxin sites interconvert between $S = 0$ and open-shell $S = 1/2$ states. The dominance of antiferromagnetic over ferromagnetic coupling of the high-spin iron ions [4] has been attributed to result from the covalent bonding along the Fe–sulfido–Fe linkages, rendering the mixed-valent $S = 1/2$ form $[Fe(III)(\mu\text{-}S)_2Fe(II)]^+$ energetically favorable [2,5].

Whereas the understanding of the relationship between biological function and electronic properties of closed- and open-shell forms of Cu_A and 2Fe-ferredoxins has been widely developed, details on the mechanism of formation and of the parameters that control structural persistence of $[M_2(\mu\text{-}S)_2]$ sites have remained largely unknown. In vitro studies starting from an apoprotein concluded that Cu_A assembles rapidly in form of its open-shell state after stepwise introduction of Cu(I) and Cu(II) sites [6–9]. Different from natural Cu_A, preparative assembly of the bimetallic core $[Cu_2(\mu\text{-}S)_2]$ commonly involves dimerization of homovalent precurors [10–13]. Analogous studies on binuclear cores of iron are scare [14,15], whereas preparation of molecular model structures involves ligand exchange at a preformed $[Fe_2(\mu\text{-}S)_2]$ core [4,16–22]. According to recent mechanistic work, the ligand environment and the overall oxidation state determine the structural dynamics of the $[Fe_2(\mu\text{-}S)_2]$ core, for which S = S^{2-} [23].

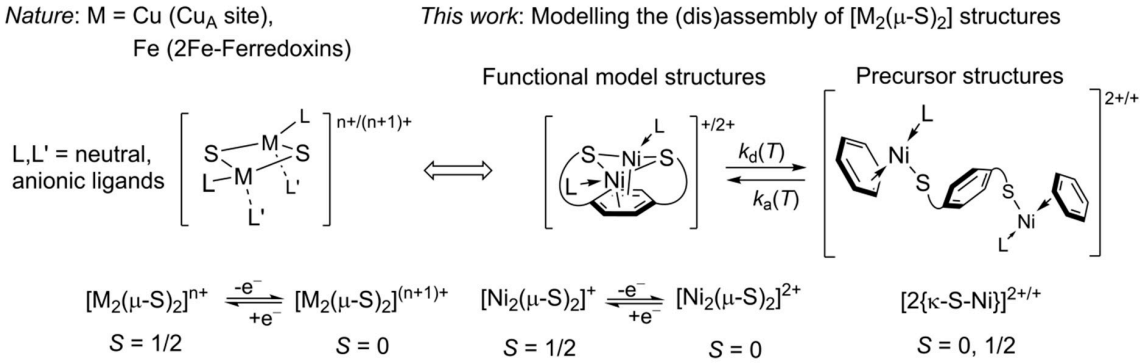

Figure 1. Comparison of geometric and electronic structures of natural bimetallic sites of the general type $[M_2(\mu\text{-}S)_2]$ with a set of four bimetallic model structures of nickel.

Gaining a quantitative understanding of the (dis)assembly of $[M_2(\mu\text{-}S)_2]$ sites is of fundamental interest. Mechanistic work in this context requires a ligand platform that suits to stabilize precursor structures in which the metal sites are independent and can exist in different oxidation states. As depicted in Figure 1, alignment of two mesityl substituted thiophenol donors at a 1,4-disubstituted arene provides a ligand framework for which both types of structures have been accessed. The set of four bimetallic complexes of nickel comprises $S = 0$ and mixed-valent $S = 1/2$ forms $[Ni_2(\mu\text{-}S)_2]^{+/2+}$, S = Aryl-$S^-$, in addition to $[2\{\kappa\text{-}S\text{–}Ni\}]^{2+/+}$ in which the nickel fragments are structurally independent. The capability of nickel to adopt tetrahedral and T-shaped ligand fields in addition to $\eta^{2/3}$-binding of an aromatic π-system is critical. A phosphine coligand L completes the coordination sphere at nickel. A previous study revealed that all redox state changes are electrochemically reversible at potential sweep rates $\nu \leq 2000$ mV·s^{-1} in 0.1 M $n$$Bu_4NPF_6$/1,2-$C_6H_4F_2$ solution at 24 °C [24]. The homovalent, $S = 0$, form of $[Ni_2(\mu\text{-}S)_2]^{2+}$, Ni = Ni(II), is metastable and rearranges into $[2\{\kappa\text{-}S\text{–}Ni\}]^{2+}$. The barrier for this process varies sensitively with the steric demand of the coligand L as half-lives decrease in the order $t_{1/2,d}$ = hours (L = $P(C_6H_{11})_3$) >> 730 s (PPh_3) > 5 s (PMe_3). In agreement with studies on the formation of Cu_A, structural assembly of the open-shell form $[Ni_2(\mu\text{-}S)_2]^{+}$ is kinetically substantially favored over dissociation of the homovalent congener. Digital simulation of cyclic voltammetry (CV) current-potential (*i*-*E*) curves established that $[2\{\kappa\text{-}S\text{–}Ni\}]^{+}$, which consists of Ni(II) and Ni(I) fragments, converts into $[Ni_2(\mu\text{-}S)_2]^{+}$ on a time scale $t_{1/2,a} < 0.001$ s at 24 °C. The metastable character of homovalent $[Ni_2(\mu\text{-}S)_2]^{2+}$, Ni = Ni(II), is a critical property, considering that structural persistence of the $[M_2(\mu\text{-}S)_2]$ core in both $S = 0$ and 1/2 states is essential to biological function.

The formation of $[Ni_2(\mu\text{-}S)_2]^{+}$ from $[2\{\kappa\text{-}S\text{–}Ni\}]^{+}$ is thermodynamically highly favored on account of a difference of ~1 V between respective formal redox potentials [24]. However, the markedly higher rate of formation of $[Ni_2(\mu\text{-}S)_2]^{+}$ appears to result from a kinetic effect. The proposal of a kinetic contribution considers that the spatial alignment of the two metal fragments in the transition state should benefit from a higher degree of freedom that arises from divergent stereoelectronic preferences of the metal ions. The lower effective core charge of Ni(I) renders changes of its coordination geometry

and number energetically less demanding than for Ni(II), which should manifest in respective transition state energies. We herein report circumstantial evidence in support of such a kinetic contribution. Substitution of previously employed coligands L = PMe_3 and PPh_3 for PMe_2Ph is reported to result in an increase of the rate of disassembly of $[Ni_2(\mu\text{-}S)_2]^{2+}$, Ni = Ni(II), at low temperatures as well as of the rate of formation of $[Ni_2(\mu\text{-}S)_2]^{+}$, Ni = Ni(I)/Ni(II), from $[2\{\kappa\text{-}S\text{–}Ni\}]^{+}$. Quantitative analysis of kinetic and electrochemical data indicate that the conversion of metastable $[Ni_2(\mu\text{-}S)_2]^{2+}$ into $[2\{\kappa\text{-}S\text{–}Ni\}]^{2+}$ involves the weakening of the dative bond between Ni and coligand L, and that the steric properties of L affect the barrier to formation of the mixed-valent sulphur-bridged structure.

2. Results

2.1. Preparation and Characterization of Bimetallic Compounds

As shown in Figure 2, compound **$[Ni_2(\mu\text{-}S)_2]^{+}$** has been prepared in form of its $N(SO_2CF_3)_2$, NTf_2, salt following a two-step procedure that starts from mononuclear complex **Ni–2S**. Complex **Ni–2S** is isostructural to the PMe_3 ligated congener [24] in the solid state and in solution. ^1H and $^{13}C\{^1H\}$ NMR spectra in $CDCl_3$ solution display N-line splitting patterns for the carbon nuclei at methyl and the quaternary position of the phenyl group of the coligand, which corroborates *trans*-disposition of PMe_2Ph at nickel. The reaction of **Ni–2S** and $Ni(cod)_2$, cod = 1,5-cyclooctadiene, in toluene solution at ambient temperature affords the bimetallic complex **2Ni–2S** almost quantitatively. Product **2Ni–2S** can be isolated from saturated pentane solutions as a dark yellow microcrystalline solid in moderate yield of about 50%. To avoid the loss of product owing to high solubility, **2Ni–2S** is oxidized in situ using $[Fc]^+$, Fc = ferrocene, affording **$[Ni_2(\mu\text{-}S)_2]^{+}$** in 80% crystalline yield.

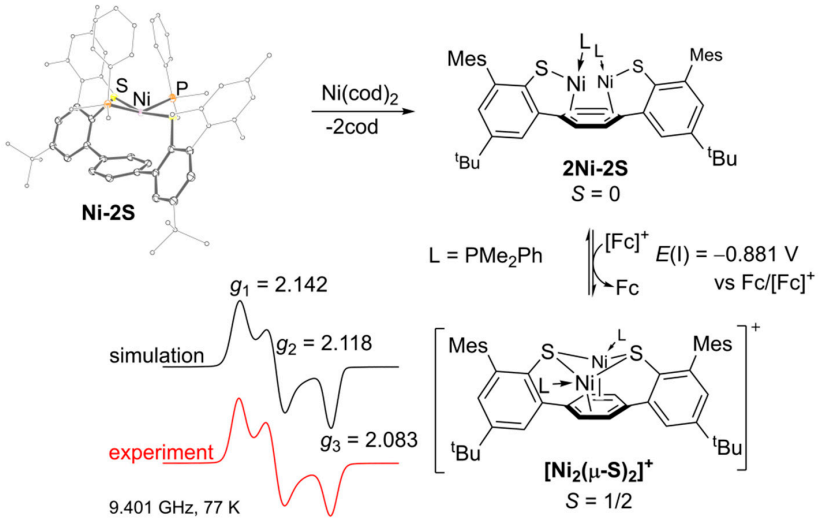

Figure 2. Preparation, molecular structures, and selected properties of mono- and bimetallic complexes of nickel; $N(SO_2CF_3)_2$ counteranion of **$[Ni_2(\mu\text{-}S)_2]^{+}$** and H-atoms in ORTEP representation of **Ni–2S** omitted for clarity; X-Band cw-EPR spectrum recorded from 2-methyltetrahydrofuran glass at 77 K, *g*-factors determined by digital simulation; Fc = ferrocene, and cod = 1,5-cyclooctadiene.

Single crystal X-ray diffraction (XRD) analysis confirmed the skeletal connectivity of **$[Ni_2(\mu\text{-}S)_2]^{+}$** as drawn in Figure 2. Despite moderate resolution of diffraction data impaired structure refinement to a high level of accuracy, PMe_2Ph ligated **$[Ni_2(\mu\text{-}S)_2]^{+}$** is isostructural to its PMe_3 congener [24]; pertinent data are provided in the Supplementary Material. Short Ni–C distances of ~2.01 Å point to a η^2:η^2-coordination of the 1,4-disubstituted π-system to the nickel atoms. Coordination of two thiophenolates in μ-fashion in addition to the PMe_2Ph coligand completes a distorted tetrahedral ligand environment at each nickel atom. Acute Ni–(μ-S)–Ni bond angles of ~63° render the Ni–Ni distance short at 2.366(3) Å. Tetrahedral metal coordination implies the presence of an *S* = 1 Ni(II) and

an $S = 1/2$ Ni(I) site. X-Band cw-EPR spectra recorded from a 2-methyltetrahydrofuran solution at 293 and 77 K corroborate a total $S = 1/2$ system that results from formal antiferromagnetic coupling of $S = 1$ and $S = 1/2$ configured nickel ions. As depicted in Figure 2, the spectrum of a frozen sample is of rhombic appearance. The g-factor at highest field, $g_3 = 2.08$, deviates substantially from the electron free-spin g-factor, $g_e \sim 2.00$, but g-anisotropy, $\Delta g = 0.06$, is small. Considering that hyperfine coupling to any of the two ^{31}P nuclei is not resolved, EPR data point to a predominant localization of the unpaired electron at nickel, sulphur, and likely the 1,4-disubstituted π-system. A mixed-valent description $[Ni(I)(\mu\text{-}S)_2Ni(II)]^+$ is preferred but the homovalent form $[Ni(1.5)_2(\mu\text{-}S)_2]^+$ cannot be excluded. The orange appearance of diluted solutions of **$[Ni_2(\mu\text{-}S)_2]^+$** in CH_2Cl_2 results from moderately intense transitions at $\lambda(\varepsilon/M^{-1}\cdot cm^{-1}) = 567$ (4200) and 773 nm (2500).

Bulk oxidation of either **2Ni–2S** or **$[Ni_2(\mu\text{-}S)_2]^+$** by a 1:2 equivalents mixture of benzoquinone and $HN(SO_2CF_3)_2$ in 1,2-$C_6H_4F_2$ solution affords the NTf_2 salt of **$[2\{\kappa\text{-}S\text{–}Ni\}]^{2+}$** that was isolated as an orange powder in 60–70% yield. Monitoring the reaction of **$[Ni_2(\mu\text{-}S)_2]^+$** and the 1,1′-diacetylferrocene cation, $[Fc'']^+$, by NMR spectroscopy in CD_2Cl_2 solution at $T \leq -60$ °C did not allow detecting **$[Ni_2(\mu\text{-}S)_2]^{2+}$** as the initial product of oxidation but **$[2\{\kappa\text{-}S\text{–}Ni\}]^{2+}$** was observed exclusively in a 1:1 molar ratio to Fc″ coproduct. The diamagnetism of **$[2\{\kappa\text{-}S\text{–}Ni\}]^{2+}$** points to a T-shaped ligand field at Ni(II), comprising κ-thiophenolate, *cis*-PMe_2Ph and the π-system of the flanking mesityl group as donors. $^{13}C\{^1H\}$ NMR solution data are in agreement with η^3-coordination of Ni(II) to the mesityl group in *trans*-position to PMe_2Ph by the presence of doublet resonances for mesityl *ipso*-^{13}C ($J_{C,P} = 8$ Hz; $\delta(C_{ipso}) = 121$ ppm) and equivalent *ortho*-^{13}C nuclei ($J_{C,P} = 2$ Hz). The presence of structurally independent Ni(II) sites is augmented by a low intensity ligand field transition at $\lambda(\varepsilon/M^{-1}\cdot cm^{-1}) = 872$ (200) nm in UV–VIS spectra, which replaces the transition of starting material **$[Ni_2(\mu\text{-}S)_2]^+$** at 773 nm (2500 $M^{-1}\cdot cm^{-1}$). NMR spectroscopic and UV–VIS absorption data of **$[2\{\kappa\text{-}S\text{–}Ni\}]^{2+}$** match those of the mononuclear congener **$[\kappa\text{-}S\text{–}Ni]^+$**, for which $\lambda(\varepsilon/M^{-1}\cdot cm^{-1}) = 915$ (100) nm and $\delta(C_{ipso}) = 123$ ppm (doublet with $J_{C,P} = 8$ Hz). The molecular structure of a single-crystalline sample of **$[\kappa\text{-}S\text{–}Ni]^+$** confirmed pertinent structural properties as depicted in Figure 3. A property of **$[\kappa\text{-}S\text{–}Ni]^+$** that is notable in regard to the rearrangement of **$[Ni_2(\mu\text{-}S)_2]^{2+}$** into **$[2\{\kappa\text{-}S\text{–}Ni\}]^{2+}$** is the migration of the Ni(II)-L fragment between the two mesityl π-systems that occurs slowly on the NMR time scale at $T = 26$ °C according to ^1H-^1H-ROESY (Rotating frame Overhauser Enhancement SpectroscopY) data.

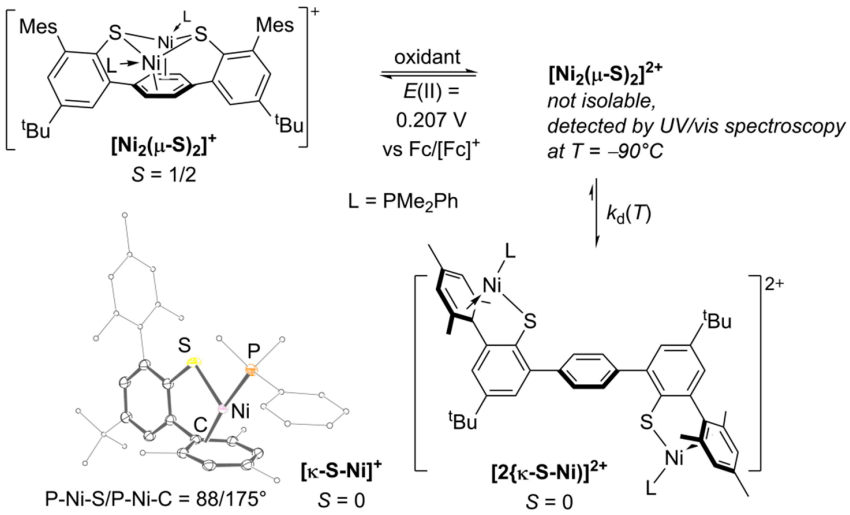

Figure 3. Preparation and molecular structure of bimetallic **$[2\{\kappa\text{-}S\text{–}Ni\}]^{2+}$**, and molecular structure of mononuclear reference complex **$[\kappa\text{-}S\text{–}Ni]^+$**; alternatively, **2Ni–2S** can substitute **$[Ni_2(\mu\text{-}S)_2]^+$** as starting material; $N(SO_2CF_3)_2$ counteranions, and H-atoms in ORTEP representation of **$[\kappa\text{-}S\text{–}Ni]^+$** omitted for clarity; oxidant = 1,1′-diacetylferrocenium–$N(SO_2CF_3)_2$ or 1:2 equivalents mixture of benzoquinone and $HN(SO_2CF_3)_2$; Fc = ferrocene.

2.2. Quantitative UV–VIS Spectroscopic Study of Oxidation-Induced Disassembly of $[Ni_2(\mu\text{-}S)_2]^+$

Probing the reaction of $[Ni_2(\mu\text{-}S)_2]^+$ and $[Fc'']^+$ by NMR spectroscopy revealed that $[Ni_2(\mu\text{-}S)_2]^{2+}$ is short-lived even at $T \leq -60$ °C. Rapid formation of $[2\{\kappa\text{-}S\text{–}Ni\}]^{2+}$ under these conditions contrasts the reactivity of the PMe_3 ligated congener that reacts noticeably at $T \geq -40$ °C [24]. For this reason, the oxidation reaction was monitored by UV–VIS spectroscopy at $T = -90$ °C in CH_2Cl_2 solution. The first absorption spectrum recorded after oxidant addition displayed an intense electronic transition centered at $\lambda(\varepsilon/M^{-1}\cdot cm^{-1}) = 715$ nm (9000). The appearance of an intense low-energy band is a characteristic feature of the $[Ni_2(\mu\text{-}S)_2]^{2+}$ core, and the position of the PMe_2Ph ligand isomer fits the order of transition energies of PMe_3 and PPh_3 ligated derivatives at 695 (7000) and 765 nm (6000), respectively [24]. Even at $T = -90$ °C, the spectral profile of PMe_2Ph ligated $[Ni_2(\mu\text{-}S)_2]^{2+}$ converts into that of $[2\{\kappa\text{-}S\text{–}Ni\}]^{2+}$. A semi-logarithmic plot of normalized concentrations of $[Ni_2(\mu\text{-}S)_2]^{2+}$ vs. time is linear, pointing to a 1st order dependence of the reaction rate on the concentration of $[Ni_2(\mu\text{-}S)_2]^{2+}$. Rate constants $k_d(T)$ were determined at $-90 \leq T \leq -50$ °C, and half-live times decreased correspondingly in the range $944 \leq t_{1/2,d} \leq 19$ s. Linear regression of a plot of $\ln(k_d(T)/T)$ vs. $1/T$ yielded $\Delta H^{\ddagger}_d = 34 \pm 2$ kJ·mol^{-1} and $\Delta S^{\ddagger}_d = -(120 \pm 25)$ J·mol^{-1}·K^{-1}. Pertinent kinetic data are provided in the Supplementary Material. Based on the activation parameters obtained, extrapolation provides $t_{1/2,d}(25\ °C) \approx 0.14$ s or $k_d(25\ °C) \approx 5$ s^{-1}, which equals an approximately three times higher reaction rate than for the PMe_3 ligated congener in CH_2Cl_2 solution; $t_{1/2,d}(25\ °C, L = PMe_3) \approx 0.35$ s or $k_d(25\ °C, L = PMe_3) \approx 2$ s^{-1}, cf. supplementary Table S3 of [24]. The decrease of $\Delta H^{\ddagger}_d$ by ≈ 50 kJ· mol^{-1} by substituting $L = PMe_3$ for PMe_2Ph is substantial but is compensated by the change of $\Delta S^{\ddagger}_d \approx -100$ J·mol^{-1}·K^{-1} that becomes dominant with increasing temperature. The lower contribution of $\Delta H^{\ddagger}_d$ to the free energy of activation indicates that a change of the properties of the dative bond between coligand L and Ni(II) determines the energy of the transition state that connects structures $[Ni_2(\mu\text{-}S)_2]^{2+}$ and $[2\{\kappa\text{-}S\text{–}Ni\}]^{2+}$. On the one hand, weakening of the L→Ni(II) bond in preparation of the transition state manifests in a higher $\Delta H^{\ddagger}_d$ but, on the other hand, reduces steric interaction between the aryl-S–Ni–L fragments during structural rearrangement, rendering $\Delta S^{\ddagger}_d$ more favorable (less negative) as observed.

Any attempt to detect $[2\{\kappa\text{-}S\text{–}Ni\}]^+$ as the initial product from the reduction of $[2\{\kappa\text{-}S\text{–}Ni\}]^{2+}$ by $(\eta^5\text{-}C_5H_5)_2Co$, and monitor its subsequent conversion into $[Ni_2(\mu\text{-}S)_2]^+$, were unsuccessful. The skeletal rearrangement of $[2\{\kappa\text{-}S\text{–}Ni\}]^+$ is subject to a small kinetic barrier, reflecting that it is facile even at $T = -95$ °C. For an independent estimation of k_a and k_d, (dis)assembly processes have been studied by cyclic voltammetry starting from $[Ni_2(\mu\text{-}S)_2]^+$.

2.3. Quantitative Electrochemical Study of Rate Constants k_a and k_d for (dis)Assembly of $[Ni_2(\mu\text{-}S)_2]^+$

Figure 4 shows a representative CV *i-E* curve recorded from solutions of $[Ni_2(\mu\text{-}S)_2]^+$ in 0.1 M nBu$_4$NPF$_6$/1,2-$C_6H_4F_2$ at a glassy carbon working electrode at 20 °C. The extended square scheme included in Figure 4 assigns the three redox events observed, which are the electrochemically reversible interconversions of $[Ni_2(\mu\text{-}S)_2]^+$/**2Ni–2S** at $E(I) = -0.881$ V and $[Ni_2(\mu\text{-}S)_2]^+/[Ni_2(\mu\text{-}S)_2]^{2+}$ at $E(II) = 0.207$ V, and the irreversible reduction of $[2\{\kappa\text{-}S\text{–}Ni\}]^{2+}$ to $[2\{\kappa\text{-}S\text{–}Ni\}]^+$ at $E_p(III,\nu = 50\ mV\cdot s^{-1}) = -0.76$ V vs. Fc/[Fc]$^+$. Contrasting coligands PMe_3 and PPh_3, substitution for PMe_2Ph limits the range of potential sweep rates at which electrochemically reversible behavior is observed to $50 \leq \nu \leq 500$ mV·s^{-1}. The peak current ratio $i_{p,red}(II)/i_{p,ox}(II)$ deviates noticeably from unity at lower potential sweep rates because the formation of $[2\{\kappa\text{-}S\text{–}Ni\}]^{2+}$ competes effectively with the reduction of electrochemically generated $[Ni_2(\mu\text{-}S)_2]^{2+}$ back to $[Ni_2(\mu\text{-}S)_2]^+$. Newly formed $[2\{\kappa\text{-}S\text{–}Ni\}]^{2+}$ is reduced at $E_p(III,\nu)$ but the subsequent skeletal rearrangement of $[2\{\kappa\text{-}S\text{–}Ni\}]^+$ into $[Ni_2(\mu\text{-}S)_2]^+$ is very rapid on the time scale of the potential sweep experiment so that no corresponding oxidation peak is observed. At $\nu \geq 500$ mV·s^{-1}, $E_p(III,\nu)$ merges with the reduction peak of $E(I)$. The shift of $E_p(III,\nu)$ to cathodic (negative) potentials with increasing scan rate is characteristic of an EC type mechanism, in which a rapid and irreversible chemical process withdraws an electrochemically generated species from a Nernst equilibrium [25]. CV *i-E* curves

recorded by scanning in cathodic potential direction are devoid of E_p(III,ν). The corresponding CV data of **[2{κ-S–Ni}]$^+$** do not display redox event *E*(II), except if the potential scan is started in cathodic direction, first traversing through E_p(III,ν) in accord with CV data for **[Ni$_2$(μ-S)$_2$]$^+$**.

A prerequisite to estimating k_a by digital simulation of *i*-*E* curves according to the extended square scheme in Figure 4 is, however, that the formal potential *E*(III) is known. To eliminate the interdependence of E_p(III,ν) and k_a, reference compound **[κ-S–Ni]$^+$** has been analyzed that interconverts electrochemically reversible with **κ-S–Ni** at *E*(III*) = −0.814 V. Assuming that *E*(III) = *E*(III*), experimental and simulated *i*-*E* curves match reasonably well as judged by the eye, except for a deviation of $i_{p,ox}$(I) that is noticed at potential sweep rates $50 \leq \nu \leq 1000$ mV·s^{-1}. Values obtained for k_d(20 °C) varied in the range of 0.6–2.2 s^{-1}, which is in good accord with k_d(20 °C) = 2.9 s^{-1} computed from activation parameters. Structural assembly of **[Ni$_2$(μ-S)$_2$]$^+$** occurs at a much higher rate than disassembly of **[Ni$_2$(μ-S)$_2$]$^{2+}$** under identical conditions and simulation provided k_a(20 °C) = (2800 ± 500) s^{-1}. The size of k_a determines the onset of E_p(III,ν) and $i_{p,red}$(I), both of which are in good to reasonable agreement with experimental CV data.

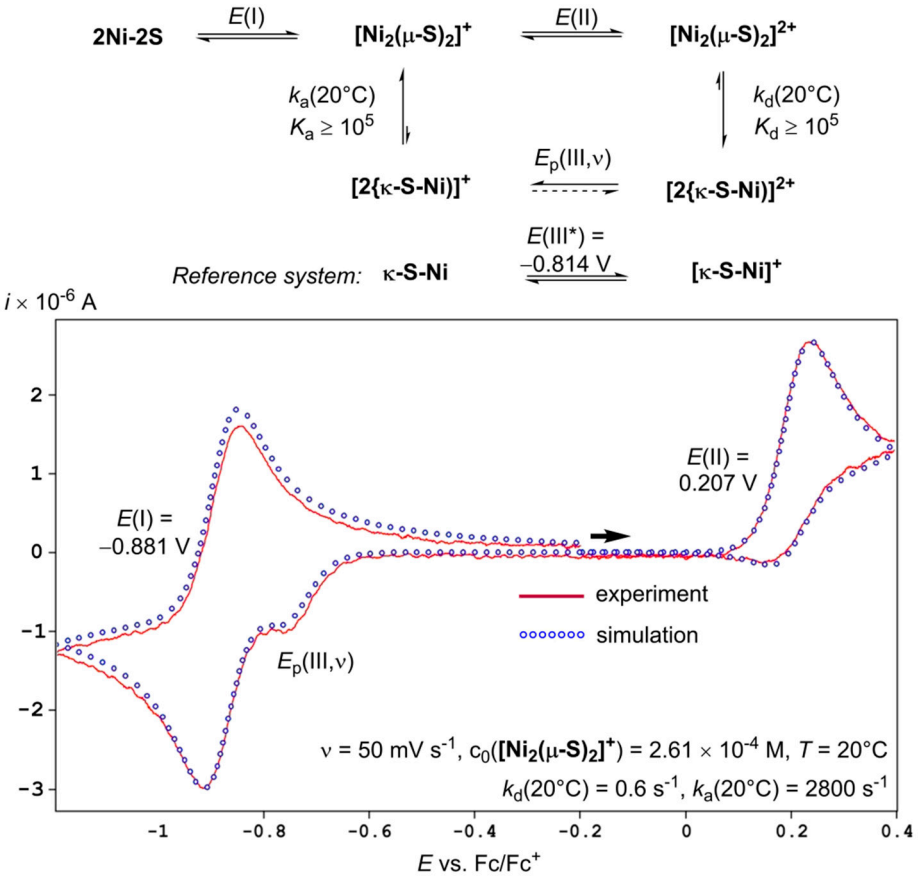

Figure 4. Digital simulation of CV *i*-*E* curves based on the extended square scheme depicted at the top; data recorded in 0.1 M nBu$_4$NPF$_6$/1,2-C$_6$H$_4$F$_2$ solution at a 0.088 cm^2 glassy carbon disc electrode, solid black arrow indicates open circuit potential and initial direction of potential sweep; Fc = ferrocene.

3. Discussion

Sulphur-bridged bimetallic structures of the general form [M$_2$(μ-S)$_2$] contribute to a variety of processes in Nature. Their biological function commonly involves the interconversion of states that differ in electronic but not geometrical structures, for which Cu$_A$ and 2Fe-ferredoxins are prominent examples. The relationship between function and electronic structure seems well understood but the mechanism of assembly of [M$_2$(μ-S)$_2$] sites has remained largely elusive. In this context, the design of molecular compounds that model function and (dis)assembly from or into precursor structures

is of fundamental interest. Combining π-systems as labile ligands with thiophenol(s) has enabled studying the redox dependent interconversion between sulphur-linked $[Ni_2(\mu\text{-}S)_2]^{+/2+}$ and structural isomers $[2\{\kappa\text{-}S\text{–}Ni\}]^{2+/+}$ that feature geometrically independent nickel sites. The phosphine coligand at nickel not only serves to saturate metal coordination but also mimics the effect that additional donor groups have on the properties of $[M_2(\mu\text{-}S)_2]$ cores. Notably, the electronic structure of $[Ni(I)(\mu\text{-}S)_2(II)]^+$ is equivalent to the $[Fe(II)(\mu\text{-}S)_2Fe(III)]^+$ form of 2Fe-ferredoxins.

The thermodynamic driving force of the formation of $[Ni_2(\mu\text{-}S)_2]^+$ equals the difference of formal potentials of redox couples $\mathbf{[Ni_2(\mu\text{-}S)_2]^{2+}/[Ni_2(\mu\text{-}S)_2]^+}$, E(II), and $\mathbf{[2\{\kappa\text{-}S\text{–}Ni\}]^{2+}/[2\{\kappa\text{-}S\text{–}Ni\}]^+}$, E(III). Computing the average over $\Delta E = E(\text{II}) - E(\text{III}) = E(\text{II}) - E(\text{III}^*)$ for all coligands L yet studied yields $\Delta E = 976 \pm 36$ mV, highlighting the distinct thermodynamically stability of the $S = 1/2$ state. The small variation of ΔE indicates that differences between activation parameters $\Delta H^{\ddagger}_{d}$ and $\Delta S^{\ddagger}_{d}$ as well as the ratio of rate constants $k_a(T)/k_d(T) \geq 10^3$ do not result from substantial differences between ground state energies but from differences between the energies of associated transition states. Studying the temperature dependence of $k_d(T)$ has provided insight into the relation between the properties of coligand L and transition state energy, which comprises two factors. The first relates to the steric properties of L whereas the second considers the properties of the dative bond between metal and L. Increasing the steric demand of L results in a higher $\Delta H^{\ddagger}_{d}$ in order to weaken the Ni←L bond in preparation of the transition state. A lower steric demand of L results in smaller $\Delta H^{\ddagger}_{d}$ but at the cost of an unfavorable contribution of $\Delta S^{\ddagger}_{d}$ that increases with increasing temperature. The second scenario seems to apply to the case of L = PMe_2Ph, for which the ratio $k_a(T)/k_d(T)$ decreases with increasing temperature. Secondary interactions such as dispersion forces and π–π-interactions between co- and primary ligand may further contribute to stabilizing the transition states.

Different from the influence of coligand L, the oxidation state of the metal is a second parameter that controls the rates of (dis)assembly processes. More precisely, the energy that is required for two S–Ni–L fragments to adopt to the transition state geometry is expected to benefit from diverging stereoelectronic properties of the nickel ions. This proposal explains the marked kinetic preference of formation of sulphur-bridged $[Ni_2(\mu\text{-}S)_2]^+$, Ni = Ni(I)/Ni(II), from geometrically independent, heterovalent nickel sites, and augments mechanistic data reported for the skeletal assembly of Cu_A [1,6–9]. This mechanism may also apply to the self-assembly of the mixed-valent form of 2Fe-ferredoxins, for which, however, experimental data are not yet available, rendering the bimetallic model structures of nickel unique. The kinetic stability of the homovalent form $[Ni_2(\mu\text{-}S)_2]^{2+}$, Ni = Ni(II), varies sensitively with the steric properties of coligand L. Comparison to Cu_A and 2Fe-ferredoxin structures in Nature points to a stabilizing contribution of neutral or negatively charged coligands. Bonding of σ-donating groups levels the effective core charges of the metal ions and limits σ-donation from sulphur donors. The increase of covalent M–S bond character would otherwise favor κ-S over μ-S-bonding and trigger dissociation of the homovalent state. The kinetic stability of the homovalent forms of Cu and Fe containing $[M_2(\mu\text{-}S)_2]$ structures, however, is essential for their biological function.

4. Materials and Methods

All manipulations of air- and moisture-sensitive compounds were carried out under an atmosphere of dry argon using standard Schlenk or glove box techniques. Literature procedures were followed for the preparation of $(Ph_3P)_2NiN(SiMe_3)_2$, ferrocenium salts, and thiophenol ligands [24,26,27]. General information on the purification of solvents and other reagents is provided in Supplementary Material. ^{1}H, ^{13}C, and ^{31}P NMR chemical shifts δ are given in ppm and scalar coupling constants J are given in Hz. ^{1}H and ^{13}C chemical shifts are referenced to residual ^{1}H and naturally abundant ^{13}C resonances of solvents whereas ^{31}P NMR chemical shifts are referenced to an external standard sample of 85% H_3PO_4 set to δ = 0. Variable temperature (VT) electronic spectra were recorded on PerkinElmer Lambda 35 and 1050 UV–VIS/NIR photospectrometers equipped with a Unisoku CoolSpeK UV USP-203-B cryostat (Nanoscore GmbH, Glashütten, Germany), using 1 cm quartz cells

with septum screw caps. Electronic absorption data were processed by Spectragryph, Software for optical spectroscopy, Version 1.2.9 (Dr. Friedrich Menges, Oberstdorf, Germany). CV was carried out at 20 °C (water bath) under an argon atmosphere using an ECi 200 potentiostat (Nordic Electrochemistry ApS, Copenhagen, Denmark) in a gas-tight, full-glass, three-electrode cell setup. The potentiostat was controlled using the EC4 DAQ (version 4.1.90.1, Nordic Electrochemistry) software, and data were treated with EC4 VIEW (version 1.2.36.1, Nordic Electrochemistry). A glassy carbon disc (Metrohm Deutschland GmbH & Co. KG, Filderstadt, Germany; electro-active area = 0.088 ± 0.002 cm^2) and a 1 mm coiled Pt-wire were employed as working and counter electrodes. A 0.5 mm Ag wire in a 0.01 M $AgClO_4$/0.1 M $n$$Bu_4NPF_6$ MeCN solution was employed as reference in a Haber-Luggin capillary/dual reference-electrode system [28]. IR compensation was applied during data collection, and CV data were corrected for background currents of electrolyte solutions for different potential sweep rates. Potentials are reported relative to E(Fc/[Fc]$^+$, 0.1 M $n$$Bu_4NPF_6$/1,2-$C_6H_4F_2$, 24 °C) = 0.197 ± 0.003 V vs. Ag/Ag^+. The electro-active area of the working electrode was calculated from Fc/[Fc]$^+$ measurements in 0.1 M $n$$Bu_4NPF_6$ solution in MeCN at various concentrations and potential sweep rates, using D(Fc/MeCN, 20 °C) = 2.40 × 10^{-5} $cm^2 \cdot s^{-1}$ [29]. Working electrode was rinsed with acetone, polished very gently with a paste of 0.3 µm alumina (Deutsche Metrohm GmbH & Co. KG, Filderstadt, Germany) in deionized water, rinsed thoroughly with plenty of deionized water, and finally acetone after each use and stored in a desiccator over P_2O_5. Periodic Fc/[Fc]$^+$ reference measurements verify the integrity of the working electrode as well as the stability of the Ag/Ag^+ reference potential. Samples for CV analysis were prepared by weighing substrate and 0.1 M $n$$Bu_4NPF_6$/1,2-$C_6H_4F_2$ into an 1 mL volumetric flask. Samples were kept under argon, and aliquots transferred to electrochemical cell using a gas-tight microliter syringe. DigiElch8 Professional (Build 8214, C3 Prozess-und Analysentechnik GmbH, Haar b. München, Germany) was used for digital simulation of CV data. Elemental analysis were done on a Vario Micro Cube system (Elementar Analysesysteme GmbH, Langenselbold, Germany). CCDC 1897416-1897417 contain the supplementary crystallographic data for this paper. These data can be obtained free of charge via http://www.ccdc.cam.ac.uk/conts/retrieving.html (or from the CCDC, 12 Union Road, Cambridge CB2 1EZ, UK; Fax: +44-1223-336033; E-mail: deposit@ccdc.cam.ac.uk). General numeration is as shown in Scheme 1.

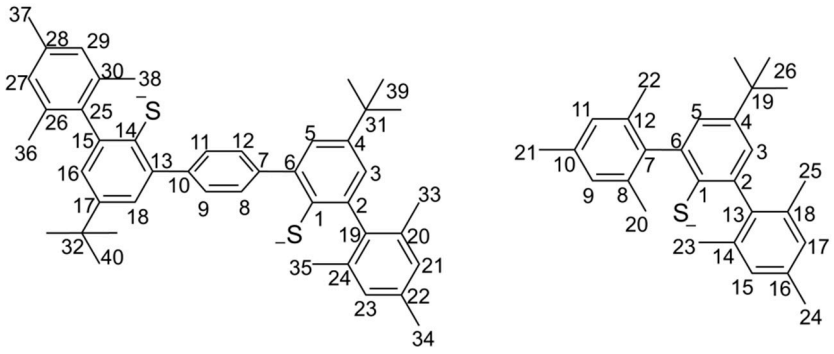

Scheme 1. Numeration of ligand frameworks in coordination compounds.

Preparation of Ni–2S. 1,4-Terphenyldithiophenol ligand (600 mg, 0.933 mmol), benzyl potassium (258 mg, 1.866 mmol), and 26 g of toluene are weighed out into a 100 mL Schlenk flask, and the mixture left stirring at r.t. until a homogeneous yellow solution results. A red solution of $(Me_2PhP)_2NiCl_2$ (378 mg, 0.931 mmol) dissolved 10 g of toluene is added by pipette, and the reaction mixture stirred overnight. A dark purple mixture resulted that was dried under dynamic vacuum, product was extracted into hexane and separated from KCl co-product by cannula filtration. The volume of combined purple hexane solutions was reduced until formation of crystals was noticed, and the mixture was stored at −30 °C overnight. Mother liquor was removed by cannula, the product was washed with methanol to remove small quantities of $OPMe_2Ph$, and finally dried under dynamic

vacuum to afford a dark purple crystalline solid (482 mg, 0.494 mmol, 53%). Slow diffusion of hexamethyldisiloxane layered on top of a solution of **Ni–2S** in toluene afforded prismatic purple single crystals that were used for X-ray diffraction and elemental analysis. ^{1}H NMR (500 MHz, $CDCl_3$, 26 °C): δ = 7.62 (s, 4H, H-8,9,11,12), 7.48 (d, 2H, $^{4}J_{H,H}$ = 2.4, H-5,18), 7.12 (m, 2H, *para*-H, Me_2P*Ph*), 7.10 (m, 4H, *ortho*-H, Me_2P*Ph*), 6.92 (m, 4H, *meta*-H, Me_2P*Ph*), 6.87 (4H, H-21,23,27,29), 6.87 (2H, H-3,16), 2.34 (s, 6H, H-34,37), 2.02 (s, 12H, H-33,35,36,38), 1.35 (s, 18H, H-39,40), 1.19 (br s, 12H, *Me*$_2$PPh); ^{13}C{^{1}H} (150 MHz, $CDCl_3$, 26 °C): δ = 143.94 (C-4,17), 142.73 (C-2,15), 141.37 (C-1,14), 140.92 (C-19,25), 140.56 (C-7,10), 138.92 (C-6,13), 136.61 (N-line pattern, $^{|1+3|}J_{C,P}$ = 38, *ipso*-C, Me_2P*Ph*), 136.11 (C-20,24,26,30), 135.3 (C-22,28), 129.96 (*ortho*-C, Me_2P*Ph*), 127.78 (*para*-C, Me_2P*Ph*), 127.53 (C-21,23,27,29), 127.36 (*meta*-C, Me_2P*Ph*), 125.98 (C-3,16), 123.52 (C-8,9,11,12), 122.12 (C-5,18), 34.16 (C-31,32), 31.52 (C-39,40), 21.17 (C-34,37), 20.61 (C-33,35,36,38), 10.95 (N-line pattern, $^{|1+3|}J_{C,P}$ = 28, *Me*$_2$PPh); ^{31}P{^{1}H} (202 MHz, $CDCl_3$, 26 °C): δ = −23.9; elemental analysis calcd (%) for $C_{60}H_{70}NiP_2S_2$: C, 73.84; H, 7.23; S, 6.57; found: C, 73.69; H, 6.76; S, 6.46; unit cell parameters: *a* = 10.7068(3), *b* = 16.6627(6), *c* = 17.9475(9) Å, α = 117.108(2), β = 92.836(2), γ = 106.327(2)°, *V* = 2675.49(19) Å^3, *Z* = 2, *P*−1, deposition number CCDC 1897416.

Preparation of 2Ni–2S. For details see preparation of **[Ni$_2$(μ-S)$_2$]$^+$**. Compound **2Ni–2S** crystallizes from saturated dark yellow solutions in pentane stored at −30 °C but yields are moderate (50–60%) owing to high solubility. ^{1}H NMR (500 MHz, C_6D_6, 26 °C): δ = 11.31 (s, 4H, H-8,9,11,12), 8.01 (d, 2H, $^{4}J_{H,H}$ = 2.4, H-3,16), 7.94 (d, 2H, $^{4}J_{H,H}$ = 2.3, H-5,18), 7.30 (m, 4H, *ortho*-H, Me_2P*Ph*), 7.07 (m, 4H, *meta*-H, Me_2P*Ph*), 6.98 (4H, H-21,23,27,29), 6.85 (tt, 2H, *para*-H, Me_2P*Ph*), 2.35 (s, 6H, H-34,37), 2.21 (s, 12H, H-33,35,36,38), 1.99 (s, 12H, *Me*$_2$PPh), 1.27 (s, 18H, H-39,40); ^{13}C{^{1}H} (150 MHz, C_6D_6, 26 °C): δ = 163.24 (br s, $\nu_{1/2}$ ~24 Hz, C-7,10), 160.96 (C-2,15), 151.97 (C-4,17), 148.62 (C-6,13), 142.85 (C-19,25), 141.33 (*ipso*-C, Me_2P*Ph*), 137.26 (C-20,24,26,30), 135.87 (C-22,28), 133.64 (*ortho*-C, Me_2P*Ph*), 129.54 (*para*-C, Me_2P*Ph*), 128.3 (*meta*-C, Me_2P*Ph*, obscured by C_6D_6), 128.2 (C-21,23,27,29, obscured by C_6D_6), 126.76 (C-3,16), 125.15 (C-5,18), 125.07 (C-8,9,11,12), 121.22 (br s, C-1,14), 33.54 (C-31,32), 32.69 (C-39,40), 21.85 (C-33,35,36,38), 21.17 (C-34,37), 16.63 (*Me*$_2$PPh); ^{31}P{^{1}H} (243 MHz, C_6D_6, 26 °C): δ = −24.4.

Preparation of [Ni$_2$(μ-S)$_2$]$^+$. (A) Preparation of **2Ni–2S**: $Ni(cod)_2$ (84 mg, 0.304 mmol) and **Ni–2S** (300 mg, 0.307 mmol) were weighted out into a 20 mL screw cap vial and 50 mL Schlenk flask, respectively, and dissolved in a total of 7 g of toluene at r.t. The solution of $Ni(cod)_2$ was transferred by pipette, and the mixture stirred for 3 h at r.t. to afford a dark yellow solution. All volatiles were removed under dynamic vacuum, the dark residue was redissolved in 7 g of toluene, and the solution stirred at r.t. overnight. All volatiles were removed again under dynamic vacuum, the residue dissolved in 7 g of THF, and this solution cooled to −30 °C in an dry ice/acetone bath. (B) Oxidation of **2Ni–2S**: A dark blue solution of $[Fc]NTf_2$ (93 mg, 0.199 mmol) was prepared in 7 g of THF in a 25 mL Schlenk flask, and the solution cannula transferred to the cold solution of **2Ni–2S**, which caused an immediate color change to a maroon appearance. After stirring for 1 h at r.t. and removal of volatiles under dynamic vacuum, the residue was washed with hexane (10 mL, 4×), dried under dynamic vacuum, and the residual maroon powder dissolved in 15 mL of 1,2-$C_6H_4F_2$, the solution filtered, volume reduced to about 5 mL, and layered with 20 mL of pentane. Pentane diffusion was complete within four days, affording a dull red crystalline solid that isolated from the mother liquor, washed with pentane, and finally dried under dynamic vacuum. Yield: 321 mg (0.244 mmol, 80%). Single crystals for X-ray diffraction analysis were obtained by layering a concentrated CH_2Cl_2 solution with pentane but moderate resolution of diffraction data did only establish skeletal connectivity; cf. supplementary Figure S3. X-Band cw-EPR (2-methyltetrahydrofuran, 3321/400 G = center/width): 293 K, 9.8359 GHz, 4 G modulation amplitude, 0.2 mW microwave power, g_{iso} = 2.116, full line width at half maximum = 0.86/3.51 mT (Gaussian + Lorentzian); 77 K, 9.4008 GHz, 1 G modulation amplitude, 0.5 mW microwave power, g_1 = 2.142, g_2 = 2.118, g_3 = 2.083; full line width at half maximum = 1.42/0.13 mT (Gaussian + Lorentzian), HStrain (EasySpin parameter to account for orientation dependent line broadening) = 11, 21, 1 MHz; UV–VIS (CH_2Cl_2, 20 °C): λ(ε/M^{-1}·cm^{-1}) = 401 (14500), 480 (5400), 567

(4200), 773 (2500) nm; elemental analysis calcd (%) for $C_{62}H_{70}F_6NNi_2O_4P_2S_4$: C, 56.64; H, 5.37; N 1.07; S, 9.75; found: C, 56.55; H, 5.2; N 1.64; S, 9.53; unit cell parameters: a = 9.3963(8), b = 23.8046(14), c = 28.0132(17) Å, $\alpha = 90°$, V = 6265.9(8) Å^3, Z = 4, P 21 21 21.

Characterization of $[Ni_2(\mu\text{-}S)_2]^{2+}$. Solutions of $[Ni_2(\mu\text{-}S)_2]^{+}$ and [Fc″]NTf_2 in CH_2Cl_2 were freshly prepared for each measurement from CH_2Cl_2 kept at 20 °C using a water bath and thermometer. An aliquot of $[Ni_2(\mu\text{-}S)_2]^{+}$ was transferred by microliter syringe to a cuvette charged with 2.6 mL of neat CH_2Cl_2, and a spectrum was recorded at 20 °C to determine sample concentration. After cooling to the desired temperature, an aliquot of oxidant solution was added under stirring, and the reaction monitored by recording the absorbance, $A(\lambda,T)$, at λ = 714 nm at defined time intervals. The change of sample volume at T < 20 °C was corrected by once recording spectra at all temperatures of interest, and doing a polynomial regression of a plot of $A(\lambda,T)$ vs. T. (UV–VIS (CH_2Cl_2, $c_0([Ni_2(\mu\text{-}S)_2]^{+}) = 8 \times 10^{-5}$ M, −90 °C): $\lambda(\varepsilon/M^{-1}\cdot cm^{-1})$ = 416 (15000), 502 (11000), 615 (shoulder, 5800), 714 (9000) nm.

Preparation of $[2\{\kappa\text{-}S\text{-}Ni)]^{2+}$. Bimetallic **2Ni–2S** was prepared from **Ni–2S** (200 mg, 0.205 mmol) and $Ni(cod)_2$ (56 mg, 0.203 mmol) as described above, and finally dissolved in 10 mL of 1,2-$C_6H_4F_2$. Alternatively, $[Ni_2(\mu\text{-}S)_2]^{+}$ can be used as the starting material. Benzoquinone (24 mg, 0.222 mmol) and $HN(SO_2CF_3)_2$ (112 mg, 0.398 mmol) were weighed out into a 50 mL Schlenk flask, immediately cooled to −30 °C in a dry ice/acetone bath, and taken up in 5–10 mL of 1,2-$C_6H_4F_2$, affording a clear yellow solution after slow warming to r.t. The oxidant solution was cannula transferred to the −30 °C cold solution of **2Ni–2S**, and the mixture stirred at r.t. for 1.5 h, yielding a bright red solution. Volatiles were removed under dynamic vacuum, the residual solid washed with diethyl ether (15 mL, 3×), and finally dried to afford a dark orange powder (200 mg, 0.125 mmol, 61% with respect to **Ni–2S**). ^{1}H NMR (500 MHz, CD_2Cl_2, −40 °C, sample prepared in situ in an NMR tube from $[Ni_2(\mu\text{-}S)_2]^{+}$ and [Fc″]$^+$ at $T \leq -78$ °C): δ = 7.67 (s, 4H, H-8,9,11,12), 7.61 (m, 4H, *ortho*-H, Me_2P*Ph*), 7.56 (m, 2H, *para*-H, Me_2P*Ph*), 7.54 (m, 4H, *meta*-H, Me_2P*Ph*), 7.24 (d, 2H, $^4J_{H,H} \approx 2$, H-5,18), 7.16 (d, 2H, $^4J_{H,H} \approx 2$, H-3,16), 7.02 (4H, H-21,23,27,29), 2.27 (s, 12H, H-33,35,36,38), 1.61 (d, $^2J_{H,P}$ = 12, 12H, *Me*$_2$PPh), 1.30 (s, 18H, H-39,40), 1.09 (s, 6H, H-34,37); $^{13}C\{^1H\}$ (150 MHz, CD_2Cl_2, 26 °C): δ = 138.47 (C-7,10), 134.76 (C-2,15), 149.17 (C-4,17), 142.03 (C-6,13), 121.36 (d, $^2J_{C,P}$ = 8, C-19,25), 129.31 (d, $^1J_{C,P}$ = 48, *ipso*-C, Me_2P*Ph*), 127 (d, $J_{C,P}$ = 2, C-20,24,26,30), 118.33 (C-22,28), 130.3 (d, $^2J_{C,P}$ = 10, *ortho*-C, Me_2P*Ph*), 132.09 (d, $^4J_{C,P}$ = 3, *para*-C, Me_2P*Ph*), 129.42 (d, $^3J_{C,P}$ = 10, *meta*-C, Me_2P*Ph*), 117.25 (C-21,23,27,29), 123.24 (C-3,16), 127.54 (C-5,18), 129.15 (C-8,9,11,12), 142.26 (d, $^3J_{C,P}$ = 10, C-1,14), 34.31 (C-31,32), 30.93 (C-39,40), 19.26 (C-33,35,36,38), 18.57 (C-34,37), 13.07 (d, $^1J_{C,P}$ = 35, *Me*$_2$PPh); $^{31}P\{^1H\}$ (243 MHz, CD_2Cl_2, 26 °C): δ = −0.16; UV–VIS (CH_2Cl_2, 20 °C): $\lambda(\varepsilon/M^{-1}\cdot cm^{-1})$ = 320 (24000), 466 (6300), 872 (200) nm; elemental analysis calcd (%) for $C_{64}H_{70}F_{12}N_2Ni_2O_8P_2S_6$: C, 48.2; H, 4.42; N 1.76; S, 12.06; found: C, 47.42; H, 3.88; N, 1.86; S, 11.72, the noticeably lower than calculated carbon and hydrogen contents appear to scale with the high relative fluorine content F, 14.3.

Preparation of $[\kappa\text{-}S\text{–}Ni]^{+}$. 4-^{t}Bu-2,6-$(Mes)_2C_6H_2SH$ ligand (150 mg, 0.373 mmol) and $(Ph_3P)_2NiN(SiMe_3)_2$ (277 mg, 0.373 mmol) were weighted out into a 20 mL screw cap vial and 50 mL Schlenk flask, respectively, and dissolved in a total of 8 g of toluene at r.t. The ligand solution was transferred by pipette, and the mixture stirred for 1.5 h at r.t. to afford a bright red solution. Volatiles were removed under dynamic vacuum, and a dark red residue was dissolved in ~15 mL of hexane. A bright red solid separated from the initially homogeneous solution at r.t., was separated from the yellow supernatant by cannula, washed with pentane (10 mL, 2×), dried under dynamic vacuum, and finally dissolved in 4 g of toluene. A purple solution of [Fc″]NTf_2 (148 mg, 0.317 mmol) was prepared in 4 g of 1,2-$C_6H_4F_2$, and transferred by pipette at r.t., affording an orange solution that was stirred for another 0.5 h. Toluene was removed under dynamic vacuum, the residual orange solid washed with pentane (10 mL, 4×), separated from the supernatant by cannula filtration, dried under dynamic vacuum, and finally dissolved in 6 g of toluene. Neat PMe_2Ph (64 μL, 0.447 mmol) was added by syringe at r.t., and the resulting dark red solution stirred for 3.5 h. Removal of solvent left a mixture of the solid product and a dark red oil. Washing with toluene (5 mL, 3×), pentane (10 mL, 3×), and

drying under dynamic vacuum afforded the product in form of an orange powder (125 mg, 0.142 mmol, 45% with respect to [Fc"]NTf_2). Layering a CH_2Cl_2 solution of the product with toluene afforded dark red plate-shaped single crystals suitable for X-ray diffraction analysis. Diffusion of pentane afforded orange needles used for elemental analysis. ^{1}H NMR (500 MHz, CD_2Cl_2, 26 °C): δ = 7.60 and 7.55 (m each, 2H each, *ortho*/*meta*-H, Me_2PPh), 7.59 (m, 1H, *para*-H, Me_2PPh), 7.19 (d, 1H, $^4J_{H,H}$ = 2, H-3), 7.05 (br s, 2H, H-9,11, η^3-mesityl), 7.00 (d, 1H, $^4J_{H,H}$ = 2, H-5), 6.92 (br s, 2H, H-15,17), 2.29 (s, 3H, H-24), 2.28 (s, 6H, H-19,22, η^3-mesityl), 1.96 (s, 6H, H-23,25), 1.58 (d, $^2J_{H,P}$ = 12, 6H, Me_2PPh), 1.33 (s, 9H, H-26), 1.25 (s, 3H, H-20, η^3-mesityl); $^{13}C\{^1H\}$ (150 MHz, CD_2Cl_2, 26 °C): δ = 150.29 (C-4), 144.53 (d, $^3J_{C,P}$ = 9, C-1), 143.13 (C-6), 137.77 (C-16), 136.86 (C14,18), 135.71 (C-13), 134.7 (C-2), 132.71 (d, $^4J_{C,P}$ = 3, *para*-C Me_2PPh), 130.9 and 130.15 (d each, $^{2,3}J_{C,P}$ = 10, 11, *ortho*/*meta*-C Me_2PPh), 130.43 (d, $^1J_{C,P}$ = 49, *ipso*-C Me_2PPh), 128.68 (C-15,17), 127.91 (C-5), 127.66 (C8,12, η^3-mesityl), 123.34 (C-3), 123.17 (d, $^2J_{C,P}$ = 8, C-7, η^3-mesityl), 120.27 (C-10, η^3-mesityl), 117.92 (C-9,11, η^3-mesityl), 35 (C-22), 31.71 (C-26), 21.42 (C-24), 20.5 (C-23,25), 19.62 (C-19,21, η^3-mesityl), 19.53 (C-20, η^3-mesityl), 14.03 (d, $^1J_{C,P}$ = 35, Me_2PPh); $^{31}P\{^1H\}$ (203 MHz, CD_2Cl_2, 26 °C): δ = −1.39; UV–VIS (CH_2Cl_2, 25 °C): λ(ε/$M^{-1}\cdot cm^{-1}$) = 332 (12000), 399 (shoulder, 3500), 464 (2700), 573 (shoulder 400), 915 (100) nm; elemental analysis calcd (%) for $C_{38}H_{44}F_6NNiO_4PS_3$: C, 51.95; H, 5.05; N 1.59; S, 10.95; found: C, 51.3; H, 4.91; N, 1.84; S, 10.83, the lower than calculated carbon analysis is attributed to the relatively high fluorine content F, 12.97%; unit cell parameters: a = 10.7068(3), b = 16.6627(6), c = 17.9475(9) Å, α = 117.108(2), β = 92.836(2), γ = 106.327(2)°, V = 2675.49(19) Å^3, Z = 2, $P-1$, deposition number CCDC 1897417.

5. Conclusions

A set of four bimetallic complexes of nickel is presented that provides a functional model system for mechanistic work on the skeletal (dis)assembly of structures $[M_2(\mu\text{-}S)_2]$ of Cu and Fe that are key components in natural metalloproteins. Biological function depends on the kinetic stability of the homovalent form $[M_2(\mu\text{-}S)_2]^{(n+1)+}$, whose disintegration is rendered unfavorable by increasing the energy of the transition state that leads to thermodynamically preferred but inactive structures. In marked contrast, assembly of the open-shell S = 1/2 redox-conjugate form $[M_2(\mu\text{-}S)_2]^{n+}$ is thermodynamically and kinetically substantially favored. Relevant factors are covalent bonding along M–S–M linkages, and diverging stereoelectronic preferences of the two metal sites that lower the energy of the transition state toward $[M_2(\mu\text{-}S)_2]^{n+}$ core assembly.

Supplementary Materials: The following are available online at http://www.mdpi.com/2304-6740/7/4/42/s1, Figures S1 and S2: Supplementary kinetic data; Figure S3: Supplementary structural data; Figures S4–S8 and Tables S1 and S2: Supplementary electrochemical data. Cif and checkcif files.

Author Contributions: Conceptualization: A.B.; data curation: H.S. and A.B.; formal analysis: R.A., H.E., and A.B.; funding acquisition: A.B.; investigation: R.A., H.E., H.S., and A.B.; project administration: A.B.; supervision: A.B.; validation: A.B.; writing—original draft: A.B.; writing—review and editing: A.B.

Funding: This research was funded by the Elite program for postdocs of the Baden-Württemberg Stiftung.

Acknowledgments: A.B. acknowledges Holger Bettinger and Bernd Speiser, Institut für Organische Chemie, Eberhard Karls Universität Tübingen, for access to a Lambda 1050 UV–VIS/NIR photospectrometer and discussion of CV data, respectively, and Wolfgang Bock, Institut für Anorganische Chemie, for elemental analysis.

Conflicts of Interest: The authors declare no conflict of interest.

References

1. Solomon, E.I.; Heppner, D.E.; Johnston, E.M.; Ginsbach, J.W.; Cirera, J.; Qayyum, M.; Kieber-Emmons, M.T.; Kjaergaard, C.H.; Hadt, R.G.; Tian, L. Copper Active Sites in Biology. *Chem. Rev.* **2014**, *114*, 3659–3853. [CrossRef]
2. Solomon, E.I.; Xie, X.; Dey, A. Mixed valent sites in biological electron transfer. *Chem. Soc. Rev.* **2008**, *37*, 623–638. [CrossRef] [PubMed]
3. Johnson, D.C.; Dean, D.R.; Smith, A.D.; Johnson, M.K. Structure, Function, and Formation of Biological Iron–Sulfur Clusters. *Annu. Rev. Biochem.* **2005**, *74*, 247–281. [CrossRef] [PubMed]

4. Ding, X.Q.; Bill, E.; Trautwein, A.X.; Winkler, H.; Kostikas, A.; Papaefthymiou, V.; Simopoulos, A.; Beardwood, P.; Gibson, J.F. Exchange interactions, charge delocalization, and spin relaxation in a mixed-valence di-iron complex studied by Mössbauer spectroscopy. *J. Phys. Chem.* **1993**, *99*, 6421–6428. [CrossRef]
5. Glaser, T.; Hedman, B.; Hodgson, K.O.; Solomon, E.I. Ligand K-Edge X-ray Absorption Spectroscopy: A Direct Probe of Ligand–Metal Covalency. *Acc. Chem. Res.* **2000**, *33*, 859–868. [CrossRef]
6. Wilson, T.D.; Savelieff, M.G.; Nilges, M.J.; Marshall, N.M.; Lu, Y. Kinetics of Copper Incorporation into a Biosynthetic Purple CuA Azurin: Characterization of Red, Blue, and a New Intermediate Species. *J. Am. Chem. Soc.* **2011**, *133*, 20778–20792. [CrossRef]
7. Chacón, K.N.; Blackburn, N.J. Stable Cu(II) and Cu(I) Mononuclear Intermediates in the Assembly of the CuA Center of Thermus thermophilus Cytochrome Oxidase. *J. Am. Chem. Soc.* **2012**, *134*, 16401–16412. [CrossRef]
8. Ghosh, M.K.; Basak, P.; Mazumdar, S. Mechanism of Copper Incorporation in Subunit II of Cytochrome *c* Oxidase from Thermus thermophilus: Identification of Intermediate Species. *Biochemistry* **2013**, *52*, 4620–4635. [CrossRef]
9. Chakraborty, S.; Polen, M.J.; Chacón, K.N.; Wilson, T.D.; Yu, Y.; Reed, J.; Nilges, M.J.; Blackburn, N.J.; Lu, Y. Binuclear CuA Formation in Biosynthetic Models of CuA in Azurin Proceeds via a Novel $Cu(Cys)_2His$ Mononuclear Copper Intermediate. *Biochemistry* **2015**, *54*, 6071–6081. [CrossRef]
10. Dance, I.G.; Guerney, P.J.; Rae, A.D.; Scudder, M.L. Planar bridging thiolate in $(Ph_3P)_2Cu(\mu\text{-}SPh)_2Cu(PPh_3)_2$. *Inorg. Chem.* **1983**, *22*, 2883–2887. [CrossRef]
11. Houser, R.P.; Young, V.G.; Tolman, W.B. A Thiolate-Bridged, Fully Delocalized Mixed-Valence Dicopper(I,II) Complex That Models the CuA Biological Electron-Transfer Site. *J. Am. Chem. Soc.* **1996**, *118*, 2101–2102. [CrossRef]
12. Thomas, A.M.; Lin, B.-L.; Wasinger, E.C.; Stack, T.D.P. Ligand Noninnocence of Thiolate/Disulfide in Dinuclear Copper Complexes: Solvent-Dependent Redox Isomerization and Proton-Coupled Electron Transfer. *J. Am. Chem. Soc.* **2013**, *135*, 18912–18919. [CrossRef]
13. Ording-Wenker, E.C.M.; van der Plas, M.; Siegler, M.A.; Bonnet, S.; Bickelhaupt, F.M.; Fonseca Guerra, C.; Bouwman, E. Thermodynamics of the Cu^{II} μ-Thiolate and Cu^{I} Disulfide Equilibrium: A Combined Experimental and Theoretical Study. *Inorg. Chem.* **2014**, *53*, 8494–8504. [CrossRef]
14. Boniecki, M.T.; Freibert, S.A.; Mühlenhoff, U.; Lill, R.; Cygler, M. Structure and functional dynamics of the mitochondrial Fe/S cluster synthesis complex. *Nat. Commun.* **2017**, *8*, 1287. [CrossRef]
15. Bonfio, C.; Valer, L.; Scintilla, S.; Shah, S.; Evans, D.J.; Jin, L.; Szostak, J.W.; Sasselov, D.D.; Sutherland, J.D.; Mansy, S.S. UV-light-driven prebiotic synthesis of iron–sulfur clusters. *Nat. Chem.* **2017**, *9*, 1229. [CrossRef]
16. Hagen, K.S.; Reynolds, J.G.; Holm, R.H. Definition of reaction sequences resulting in self-assembly of $[Fe4S4(SR)4]^{2-}$ clusters from simple reactants. *J. Am. Chem. Soc.* **1981**, *103*, 4054–4063. [CrossRef]
17. Do, Y.; Simhon, E.D.; Holm, R.H. Improved syntheses of tetrachlorodi-μ-sulfidodiferrate(2−) ($[Fe_2S_2Cl_4]^{2-}$) and hexachloro-μ-oxodiferrate(2−) ($[Fe_2OCl_6]^{2-}$) and oxo/sulfido ligand substitution by use of silylsulfide reagents. *Inorg. Chem.* **1983**, *22*, 3809–3812. [CrossRef]
18. Beinert, H.; Holm, R.H.; Münck, E. Iron–Sulfur Clusters: Nature's Modular, Multipurpose Structures. *Science* **1997**, *277*, 653–659. [CrossRef] [PubMed]
19. Venkateswara Rao, P.; Holm, R.H. Synthetic Analogues of the Active Sites of Iron−Sulfur Proteins. *Chem. Rev.* **2004**, *104*, 527–560. [CrossRef] [PubMed]
20. Ballmann, J.; Albers, A.; Demeshko, S.; Dechert, S.; Bill, E.; Bothe, E.; Ryde, U.; Meyer, F. A Synthetic Analogue of Rieske-Type [2Fe–2S] Clusters. *Angew. Chem. Int. Ed.* **2008**, *47*, 9537–9541. [CrossRef] [PubMed]
21. Ballmann, J.; Sun, X.; Dechert, S.; Schneider, B.; Meyer, F. A convenient ligand exchange pathway to [2Fe–2S] ferredoxin analogues. *Dalton Trans.* **2009**, 4908–4917. [CrossRef]
22. Saouma, C.T.; Kaminsky, W.; Mayer, J.M. Protonation and Concerted Proton–Electron Transfer Reactivity of a Bis-Benzimidazolate Ligated [2Fe–2S] Model for Rieske Clusters. *J. Am. Chem. Soc.* **2012**, *134*, 7293–7296. [CrossRef]
23. Bergner, M.; Roy, L.; Dechert, S.; Neese, F.; Ye, S.; Meyer, F. Ligand Rearrangements at Fe/S Cofactors: Slow Isomerization of a Biomimetic [2Fe–2S] Cluster. *Angew. Chem. Int. Ed.* **2017**, *56*, 4882–4886. [CrossRef] [PubMed]

24. Koch, F.; Berkefeld, A.; Speiser, B.; Schubert, H. Mechanistic Aspects of Redox-Induced Assembly and Disassembly of S-Bridged [2M–2S] Structures. *Chem. Eur. J.* **2017**, *23*, 16681–16690. [CrossRef] [PubMed]
25. Nicholson, R.S.; Shain, I. Theory of Stationary Electrode Polarography. Single Scan and Cyclic Methods Applied to Reversible, Irreversible, and Kinetic Systems. *Anal. Chem.* **1964**, *36*, 706–723. [CrossRef]
26. Mews, N.M.; Berkefeld, A.; Hörner, G.; Schubert, H. Controlling Near-Infrared Chromophore Electronic Properties through Metal–Ligand Orbital Alignment. *J. Am. Chem. Soc.* **2017**, *139*, 2808–2815. [CrossRef]
27. Koch, F.; Schubert, H.; Sirsch, P.; Berkefeld, A. Binuclear complexes of Ni(I) from 4-terphenyldithiophenol. *Dalton Trans.* **2015**, *44*, 13315–13324. [CrossRef]
28. Gollas, B.; Krauß, B.; Speiser, B.; Stahl, H. Design of a Single-Unit Haber-Luggin Capillary/Dual Reference-Electrode System. *Curr. Sep.* **1994**, *13*, 42–44.
29. Kuwana, T.; Bublitz, D.E.; Hoh, G. Chronopotentiometric Studies on the Oxidation of Ferrocene, Ruthenocene, Osmocene and Some of their Derivatives1. *J. Am. Chem. Soc.* **1960**, *82*, 5811–5817. [CrossRef]